*Tellus (2007), 59A, 321–335*
*Printed in Singapore. All rights reserved*



**TELLUS**

# Precipitation over multiscale terrain

*By* QINGFANG JIANG, *University of Corporation for Atmospheric Research, Monterey, CA 93943, USA*

(Manuscript received 19 June 2006; in final form 23 January 2007)

ABSTRACT

Stratiform precipitation over multiscale terrain is examined based on two-dimensional simulations of moist airflow past two-ridge terrain with a narrower ridge superposed on the windward slope of a wider ridge. It has been demonstrated that the narrower ridge could significantly modulate the precipitation intensity and distribution by inducing upslope ascent, leeside descent, and gravity waves.

Three distinct flow regimes have been identified based on simulations, namely linear, non-linear, and blocking regimes. For low terrain, the wave response is primarily linear, and more precipitation occurs over the narrower ridge. Precipitation over the major ridge is much reduced by precipitation over the narrower ridge, which decreases the moisture flux that reaches the major ridge, and by leeside descent over the narrower ridge, which limits the horizontal dimension of the updraft zone over the major ridge. In the linear regime, the total precipitation produced by the two-ridge terrain and the corresponding wide smooth ridge is comparable. For terrain of moderate heights, the wave response is non-linear and oscillation occurs with updraft and precipitation maxima alternating between the upwind slopes of the two ridges, likely due to non-linear wave–wave interaction. Strong lee waves are produced in the lee of the first ridge due to non-linear amplification and could significantly enhance precipitation over the major ridge through directly increasing the condensation rate over the upwind slope of the major ridge and through generating snow above the freezing level. Correspondingly, precipitation rates over the two ridges become comparable and the total precipitation over the two-ridge terrain is considerably larger than over the corresponding reference ridge. For higher terrain, blocking becomes significant and precipitation over the first ridge tends to detach from the terrain and propagates upstream.

Additional simulations indicate that the precipitation intensity and distribution are also sensitive to terrain geometry such as the ratio of the two ridge heights, the depth of the relative valley, and the distance between the two ridges.

## 1. Introduction

Major mountain barriers could significantly modulate precipitation over mountainous areas through dynamical processes such as upslope ascent, leeside descent and associated gravity wave activities. From early conventional observations such as Bergeron (1949) to modern field campaigns characterized by research aircraft in-situ observations and remote sensing technologies such as Mesoscale Alpine programme (MAP, Bougeault et al., 2001), and Improvement of Parameterization through Observational Verification Experiment (IMPROVE, Stoelinga et al., 2003), our knowledge of orographic precipitation has been advanced significantly. However, outstanding scientific questions remain unsolved regarding mechanisms and predictability of precipitation over complex terrain. In fact, to some degree, non-linear wave–wave interaction associated with dry stratified flow past complex topography is still not well understood, which can be further complicated by moist processes.

Correspondence.
e-mail: qingfang.jiang@nrlmry.navy.mil
DOI: 10.1111/j.1600-0870.2007.00232.x

In addition to observation-based case studies, our understanding of orographic precipitation has also been advanced by idealized studies using well-tested mesoscale models or cloud-resolving models. For example, precipitation associated with near-saturated and conditionally stable airflow past a three-dimensional hill has been examined by Jiang (2003) and Miglietta and Buzzi (2004) with focus on moist dynamics and its control on upslope precipitation. For low-terrain, they found that the upslope precipitation is proportional to the upwind terrain slope, and for high hills, windward blocking dominates and low-level flow may split. As a result, precipitation patterns tend to shift upstream and even detach from the terrain slope. Similar model configuration has been used by Jiang and Smith (2003) to study precipitation efficiency (PE) of upslope precipitation and its dependence on the terrain geometry, wind speed, and cloud physics. Based on a series of numerical simulations, they constructed a non-linear analytical precipitation model and PE was expressed in closed forms as functions of the advection timescale, $\tau_a = L/U_\circ$, where L is the horizontal length of the precipitating orographic cloud, cloud timescale, $\tau_c$, and the hydrometeor fallout timescale $\tau_f$. According to their formula, PE is largely controlled by the ratio of $\tau_a$ and $\tau_c$; PE is larger for a

larger $\tau_a/\tau_c$ as it allows more time for hydrometeors to grow into precipitable sizes. The cloud timescale $\tau_c$ was found to be sensitive to the incoming moisture flux; the larger the moisture flux, the higher the condensation rates, and the faster the hydrometeors grow accordingly. More recently, a linear precipitation model has been constructed using the above timescale concepts and has been used to study orographic precipitation over coastal mountains in Oregon. Reasonable agreement between model prediction and observations has been found (Smith and Barstad, 2004; Smith et al., 2005). The influence of vertical wind shear, terrain width, and freezing level on orographic precipitation has been examined by Colle (2004) and Colle and Zeng (2004) based on simulations of moist airflow past two-dimensional ridges. In addition to stratiform precipitation, convection excited by simple ridges or hills have been investigated by a few groups (Kirshbaum and Durran, 2004; Chen and Lin, 2005; Fuhrer and Schär, 2005).

The importance of terrain geometry in controlling precipitation intensity and distribution has been highlighted in these studies. To bridge the gap between complex three dimensional terrain in the real world and simple ridges and hills used in previous idealized studies, some recent studies used more sophisticated terrain shapes. For example, a L-shaped ridge has been used by Schneidereit and Schär (2000) and Rotunno and Ferretti (2001) to more realistically represent the Alps. More recently precipitation over a family of concave and convex ridges have been examined by Jiang (2006) and the effects of upstream flow confluence and diffluence on precipitation have been discussed.

This idealized study was motivated by the observations from MAP. Heavy precipitation often occurs over the southern flank of the Alps associated with moist air from the Mediterranean Sea impinging on the Alps. Observations indicated that precipitation distribution over the southern Alpine slope was significantly modulated by the presence of individual peaks and valleys with horizontal scales much smaller than the main Alpine ridge (e.g. Medina and Houze, 2003; Rotunno and Ferretti, 2003; Smith et al., 2003), likely through interactions of synoptic flow, direct upslope ascent and leeside descent, and gravity waves launched from individual peaks. In fact, similar terrain shapes, i.e. narrower peaks riding on the upwind slope of a wider ridge, are commonly seen in major barriers such as the Andes and the Coast Ranges of North America. As reviewed by a few authors (e.g. Smith, 1979), previous studies of orographic precipitation mostly focused on the windward enhancement associated with upslope ascent and the leeside rain shadow due to flow descent. The role of mountain waves in modulating precipitation distribution received much less attention to date. In case studies of precipitation over northern Arizona, Bruitjes and Hall (1994) noticed that synoptic precipitation patterns were significantly modified by the updrafts and downdrafts associated with mountain waves. In this study, we use the term mountain waves to refer to perturbations aloft due to buoyancy force as opposed to direct upslope ascent and leeside descent.

The objective of this study is to deepen our understanding of precipitation over terrain with multiple ridges characterized by multiple horizontal scales. Particularly, we seek answers to the following questions: (a) do small-scale peaks riding along the upwind slope of major barriers change the total precipitation, (b) how sensitive is precipitation over multiscale terrain to terrain geometry such as minor ridge heights and valley depths and (c) what are the relevant dynamical and microphysical processes that dictate precipitation distribution? The outline of the paper is as follows. The numerical setup and control parameters are described in Section 2. Linear wave response to stratified flow past two-ridge terrain is illustrated in Section 3. Results from the control set of simulations are presented in Section 4. In Section 5, sensitivity of precipitation distribution to terrain geometry is examined and the results are summarized in Section 6.

## 2. Numerical setup

### 2.1. Model description

The atmospheric component of the Navy's Coupled Ocean/Atmospheric Mesoscale Prediction System COAMPS®[1]) (Hodur, 1997) is used for this idealized study. COAMPS makes use of finite-difference approximations to represent the fully compressible, non-hydrostatic equations that govern atmospheric motions. The bulk moist physics scheme in COAMPS includes warm rain process (Kessler, 1969) and ice-phase physics based upon the work of Rutledge and Hobbs (1983, 1984) with a single moment prediction of mixing ratios for six microphysical variables (i.e. water vapour, pristine ice, snow, rain, cloud water and graupel).

The simulations are carried out in a two-dimensional grid with 1001 grid points along the wind direction and 90 levels in the vertical. The horizontal resolution is 1 km with open boundary conditions applied along the lateral boundaries. A terrain-following coordinate is used and the vertical grid is stretched with spacings varying from 100 m in the lowest 3 km to 1000 m at the model top where a radiation boundary condition is applied to minimize downward reflection of gravity waves.

The model is initialized using a single sounding, which will be illustrated in the next section, and integrated over 12 hr. The typical horizontal dimension of the terrain windward slope used in this study is of the order of 50 km and the ambient wind speed is $U_\circ = 15$ m s$^{-1}$, which yields an advection timescale $T_a \sim$ 1 h. Hence the integration time is approximately 12 times of the advection timescale.

### 2.2. Idealized terrain

The multiscale terrain is represented as two ridges aligned along the wind direction as shown in Fig. 2a and described by the

[1]COAMPS is a registered trademark of the Naval Research Laboratory

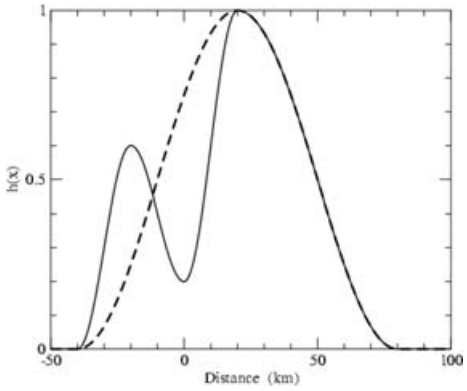


*Fig. 1.* The idealized two-ridge terrain (solid curve) and the corresponding reference ridge (dashed curve) as described by eqs. (1) and (2) with $h_m = 1$, $\alpha = 0.6$, $\beta = 0.2$, $d = 2a$, and $a = 10$ km. Note the lee slopes of the two-ridge terrain and its corresponding reference terrain are identical.

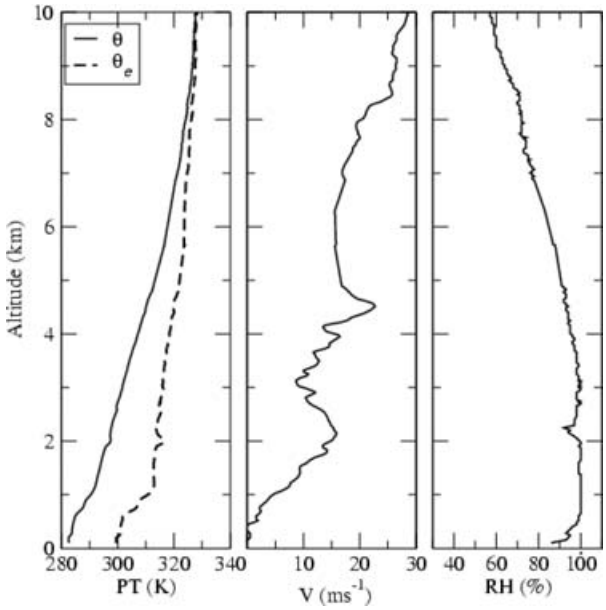


*Fig. 2.* Profiles of potential temperature ($\theta$), equivalent potential temperature ($\theta_e$), southerly component of wind, and relative humidity derived from the 12 Z 21 September 1999 Melano sounding.

following equations

$$
\begin{aligned}
h(x) &= 0, \\
&\quad \text{for } x \le -d - 2a \text{ or } x > 3d + 2a \\
&= \alpha h_m \cos^2[\pi(x + d)/(4a)], \\
&\quad \text{for } -d - 2a < x \le -d \\
&= \beta h_m + (\alpha - \beta) h_m \cos^2[\pi(x + d)/(2d)], \\
&\quad \text{for } -d < x \le 0 \\
&= \beta h_m + (1 - \beta) h_m \cos^2[\pi(x - d)/(2d)], \\
&\quad \text{for } 0 < x \le d \\
&= h_m \cos^2[\pi(x - d)/(4d + 4a)], \\
&\quad \text{for } d < x \le 3d + 2a,
\end{aligned} \tag{1}
$$

where $\alpha h_m$ and $h_m$ are the maximum heights of the first and second (major) ridge crests, $\beta h_m$ is the altitude at the lowest point between the two ridges (referred to as valley floor height hereafter), $0 < \beta \le \alpha \le 1$ are constants, and $2d$ is the distance between the two ridge crests. Clearly, the two-ridge terrain composites of four sinusoidal pieces corresponding to the upwind and downwind slopes of the two ridges, respectively. The corresponding wavelengths are $4a$, $2d$, $2d$ and $4(a + d)$, where a is taken to be 10 km in this study. Here we use the term "slope width" to refer to one-quarter of the wavelength of the corresponding slope where the terrain height is approximately 70% of the ridge crest height and "valley depth" to refer to $(\alpha - \beta)h_m$. According to (1), the upwind width of the major ridge is d and the height of the major ridge relative to the valley floor is $(1 - \beta)h_m$.

As shown in Fig. 2, a reference ridge described by

$$
\begin{aligned}
h(x) &= 0, \quad \text{for} \quad x < -d - 2a \text{ or } x > 3d + 2a \\
&= h_m \cos^2 \frac{\pi(x - d)}{4(a + d)}, \quad \text{for} \quad -d - 2a \le x \ge 3d + 2a,
\end{aligned} \tag{2}
$$

is used to represent the corresponding wider smooth ridge for comparison. Apparently, the maximum height and leeside width of the reference ridge are identical to those of the corresponding major ridge in the two-ridge terrain.

### 2.3. Idealized sounding

The idealized sounding used in this study is modified from the 1200 UTC Milano sounding obtained on 21 October 1999 during the Intensive Observational Period (IOP) 8 of the Mesoscale Alpine Programme (MAP, Bougeault et al., 2001). MAP IOP 8 was characterized by persistent stratiform precipitation over the southern Alps associated with the passage of relatively stable moist airflow from the Mediterranean Sea and has been the subject of several case studies (e.g. Chiao et al., 2004). The 1200 UTC Milano sounding has been used in idealized studies as well (Kirshbaum and Durran, 2004; Jiang, 2006). The equivalent potential temperature is computed from

$$
\theta_e = T \left(\frac{p_\circ}{p}\right)^{R_d/(c_p + c_l q_w)} \left(\frac{q_v}{q_s}\right)^{-R_v q_v/(c_p + c_l q_w)} \exp\left(\frac{L q_v}{T(c_p + c_l q_w)}\right), \tag{3}
$$

following Emanuel (1994), where T is the temperature, $p$ is the pressure, $p_\circ$ the reference sea-level pressure, $c_p$ and $c_l$ are the specific heats at constant pressure of dry air and liquid water, $R_d$ and $R_v$ are the ideal gas constants for dry air and water vapour, $L$ is the latent heat of the condensation of water, and $q_v$, $q_s$, and $q_w$ are the water vapour, saturation, and total mixing ratios, respectively.

It is evident that the troposphere is convectively stable and characterized by a two-layer structure in terms of stability; more

stable below 5 km and less stable in the upper troposphere (Fig. 2). The corresponding moist buoyancy frequency (Lalas and Einaudi, 1974) is approximately 0.01 $s^{-1}$ below 5 km and 0.006 $s^{-1}$ in the upper troposphere, respectively. The meridional component of the horizontal wind in general increases with the altitude in the troposphere with an average wind speed of approximately 15 m $s^{-1}$. For simplicity, a uniform wind speed of 15 m $s^{-1}$ is used in COAMPS simulations and therefore, vertical wind shear related dynamics is not relevant to this study.

## 3. Linear waves and scaling

Before presenting results from non-linear COAMPS simulations, we first look at a simpler problem: linear wave response to stratified flow past two-ridge terrain. Steady two-dimensional linear waves are governed the following equation

$$w_{xx} + w_{zz} + l^2 w = 0, \tag{4}$$

where $l^2 = N^2/U^2 - U_{zz}/U$ is the Scorer parameter (Scorer, 1949) and $w$ is the vertical velocity. Eq. (4) can be solved using Fast Fourier Transform (Smith, 1980) method with a linearized bottom boundary condition, $w(x, 0) = U_\circ h_x$, and a wave radiation condition aloft. Shown in Fig. 3a are the vertical velocity and streamlines of a stationary linear wave solution corresponding to a uniformly stratified flow characterized by a constant buoyancy frequency $N = 0.01$ $s^{-1}$ and a uniform wind speed $U_\circ = 15$ m $s^{-1}$, past the two-ridge terrain described by (1) with $\alpha = 0.6$, $\beta = 0.2$, $d = 2a$, and $a = 10$ km. The same set of terrain parameters are used in COAMPS simulations presented in the next section for a range of $h_m$ values. It is evident that in the lower troposphere flow ascends over the upwind slopes of both ridges and descends over the leeside slopes. Aloft, zones of updrafts are present, located over the leeside descent zones and approximately three quarters of a vertical hydrostatic wavelength (i.e. $3\pi U/2N$) above the surface, associated with vertically propagating hydrostatic waves.

As demonstrated in previous studies, the upslope ascent is particularly interesting, as it often leads to condensation of the moisture-laden low-level air flow and therefore enhances precipitation. Smith (1979) suggested that the condensation rate is proportional to the updraft w and $dq_{vs}/dz$, the vertical derivative of the saturated water vapour mixing ratio. In the absence of wave reflection above, the upslope ascent over the two upwind slopes can be approximated as

$$w(x, z) = -\frac{\pi \alpha h_r U_\circ}{4L} sin(kx + lz), \tag{5}$$

where the horizontal scale L is a for the first ridge and d for the major ridge, the relative height $h_r$ is equal to $\alpha h_m$ and $(1 - \beta)h_m$ for the first and major ridges, respectively, $k = \pi/2L$, and $l = N/U$. Within $-d - 2a \geq x \leq -d$, the vertical extension of the ascent area is $-\pi x(2al)^{-1}$. According to (5), the low-level updraft is proportional to the windward terrain slope with maxima located at the surface where the terrain slopes reach maxima. The total lifting

$$W = \rho_a \int_L dx \int_0^{-\pi x(2al)^{-1}} w(x, z)dz = \frac{\pi \rho_a h_r U_\circ^2}{2N}, \tag{6}$$

is only proportional to the relative height of the ridge and independent of the ridge width. Similarly, the total lifting over the corresponding reference ridge is $\pi(\alpha - \beta)h_m \rho_a U^2/(2N)$, and the two-ridge terrain produces more upslope lifting if only $\alpha > \beta$. It is noteworthy that the updraft zones associated with waves in the lee of the first ridge and upwind ascent over the major ridge are actually connected. In the presence of a deep moist layer, cold clouds may form due to the wave-induced updraft aloft and ice-phased hydrometeors may fall into the warm clouds below and serve as seeders to enhance precipitation over the major ridge.

Shown in Fig. 3b is the wave solution corresponding to $U =$ 15 m $s^{-1}$ and $N = 0.01$ $s^{-1}$ below 3 km, 0.006 $s^{-1}$ between 3 and 11 km, and 0.025 above 11 km, which is loosely based on the idealized sounding used in this study. The solution is derived by solving eq. (4) in each homogeneous layer separately

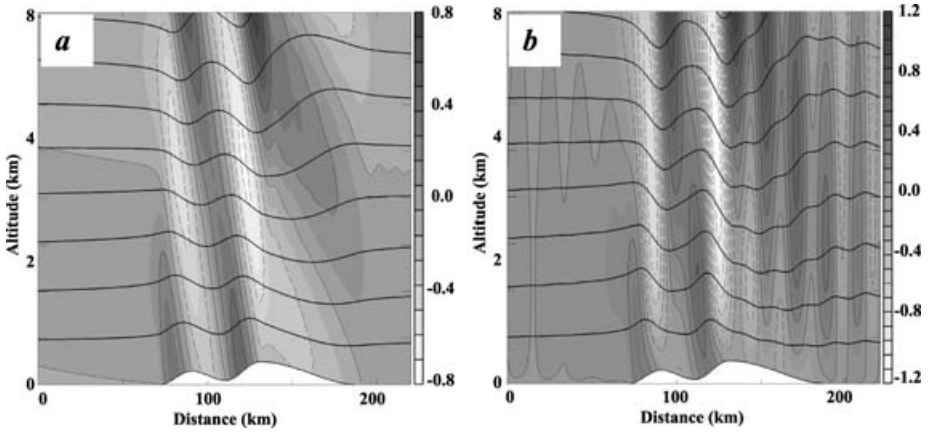


*Fig. 3.* The vertical cross-sections of the vertical velocity (greyscale, increment = 0.1 m $s^{-1}$, and thin contours, increment = 0.2 m $s^{-1}$, negative dashed) and streamlines (bold) corresponding to linear wave solutions for (a) $U_\circ = 15$ m $s^{-1}$ and $N = 0.01$ $s^{-1}$ and (b) $U_\circ = 15$ m $s^{-1}$ below 3 km and 0.006 $s^{-1}$ between 3 and 11 km, and 0.025 $s^{-1}$ above. The terrain parameters are $\alpha = 0.6$, $\beta = 0.2$, $d = 2a$, $a = 10$ km, and $h_m = 500$ m.

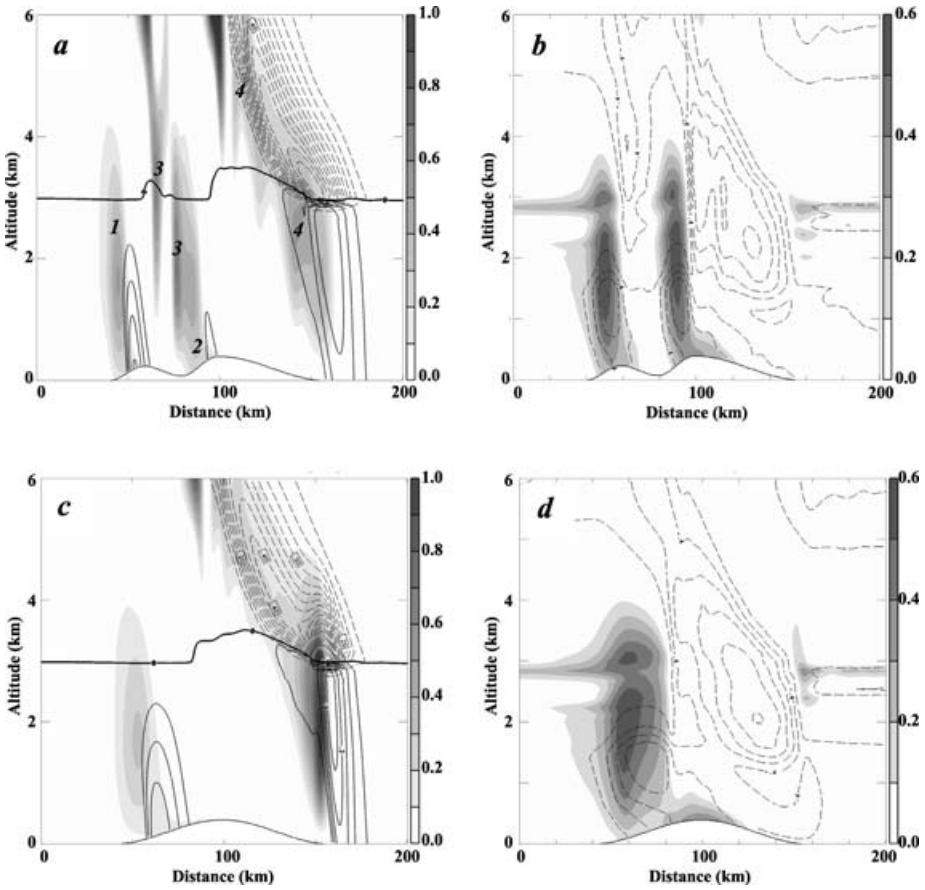


*Fig. 4.* a) Vertical cross-sections of updraft (greyscale, increment: 0.1 m s$^{-1}$), rainwater mixing ratio (solid contours, increment: 0.05 g kg$^{-1}$), and snow mixing ratio (dashed contours, increment: 0.05 g kg$^{-1}$) valid at T = 8 h, derived from the control simulations with $h_m = 400$ m. The freezing level is indicated by a bold solid curve. (b) Same vertical sections as (a) but for cloud water mixing ratio (greyscale, increment: 0.1 g kg$^{-1}$) and negative change of water vapour mixing ratio relative to the initial state (dashed contours, increment: 0.2 g kg$^{-1}$). Parts (c) and (d) same as (a) and (b), respectively, but derived from the corresponding reference simulation.

and matching pressure and vertical displacement at interfaces. Trapped wave patterns are present apparently due to the sudden decrease of the Scorer parameter at 3 km (Scorer, 1949). The wave patterns are fairly complicated due to the interference of waves launched from the two separate ridges. There are a few interesting differences between the propagating and trapped wave solutions shown in Fig. 3. The vertical extensions of the upslope ascent are considerably larger in the presence of trapped waves, apparently due to the interference between the upward propagating waves and reflected waves. Secondly, two updraft zones are located between the two ridge crests, associated with lee waves excited by the first ridge, which connect with each other and form a deep updraft area. The lower branch of the wave-induced updraft merges with the upslope ascent over the major ridge, implying its potential to directly contribute to precipitation over the major ridge. The low-level updraft maximum over the major ridge is located at approximately 2.5 km ASL, instead of at terrain surface. Again, the wave-induced updraft aloft may provide ice-phased hydrometeors in the presence of a deep moist layer.

## 4. Control simulations

In this section, we try to examine the effect of the minor ridge in modulating precipitation intensity and distribution based on diagnosis of the control set of simulations, which is defined as $d = 2a$, $\alpha = 0.6$, $\beta = 0.2$, and $a = 10$ km; the terrain parameters are identical to the linear examples shown in the previous section. The range of the mountain height $h_m$ is from 200 to 1500 m and an identical set of simulations have been performed with the corresponding reference ridges for comparison.

### *4.1. Precipitation induced by upslope ascent and lee waves*

Shown in Fig. 4 are vertical cross-sections of vertical velocity, relative humidity, and rainwater, cloud water, and snow mixing ratios derived from the control and the corresponding reference simulations for $h_m = 400$ m. For the two-ridge simulation, in the lower troposphere, there are several updraft zones (grey areas

in Fig. 4a, numbered in sequence) corresponding to the upslope ascent over the first ridge, upslope ascent over the major ridge, trapped wave downstream of the first ridge, and lee waves downstream of the major ridge, respectively. Similar to the linear wave solution shown in Fig. 3b, there are two wave-induced updraft zones located between the two ridges, and the lower one merges with the upslope ascent over the major ridge. However, unlike linear solutions, the upslope ascent maximum over the narrower ridge is located at 1.8 km above the ground, likely due to latent heat release (Smith and Lin, 1982) and wave reflection.

Precipitation occurs over the upwind slopes of the two ridges with more pronounced precipitation over the first ridge. The precipitation zones are located approximately 10 km downstream of the ascent zones due to the time lag associated with the initiation and growth of hydrometeors (i.e. rain drops here). It is interesting that although the ascents over the two ridges are comparable, the precipitation over the upwind slope of the lower ridge is much stronger than over major ridge, indicating that the PE is higher for clouds over the first ridge than over the major ridge. This can be interpreted using Figs. 4b and 5 and the PE formula give by Jiang and Smith (2003),

$$PE = (1 + \tau_c/\tau_a)^{-1}(1 + \tau_f/\tau_a)^{-1}, \quad (7)$$

where $\tau_f = H/V_t$ is the hydrometeor fallout timescale (H is the average cloud height and $V_t$ is hydrometeor terminal velocity), and $\tau_c$ is the cloud timescale, which is smaller for larger water content in the airflow. Figure 4b suggests two possible factors that likely account for the higher PE over the first ridge (see Section 5 and Fig. 8b for more discussion of PE); the wider cloud zone and the larger water vapour mixing ratio upstream of the cloud. The ascent zone (see the vertically integrated lifting and cloud water flux in Fig. 5) over the first ridge can extend upstream due to wave tilting and non-linear effects. The extent of the ascent over the major ridge is confined to the upwind slope due to the descent over the lee of the first ridge, and accordingly the advection time ($\tau_a$) is shorter. In addition, due to the precipitation over the first ridge, the water vapour mixing ratio is smaller in the airflow that reaches the major ridge, which results in a larger $\tau_c$. Accordingly, PE is smaller over the major ridge than over the first ridge.

The updraft zones over the windward slopes extend beyond the freezing level (Fig. 4a). Although no significant snow or ice cloud is shown above the freezing level, a thin line of cloud water is evident near the freezing level and extends well upstream (Fig. 4b), implying possible contribution from ice-phase clouds to precipitation over the first ridge. The updraft zones 3 correspond to trapped waves excited by the first ridge and wave clouds form accordingly. However, no rainwater is present, indicating that the updraft is not strong enough to create precipitable hydrometeors. Snow forms downstream of the updraft zones 4 over the lee of the major ridge, apparently corresponding to lee waves. Some snow falls below the freezing level and precipitates in the form of rainwater while being evaporated. For the reference ridge, the upslope ascent is weaker and more wide-spread than over the first ridge in the control simulation. Correspondingly, the precipitation is more widespread and intensity is comparable to that over the first ridge. According to (7), a wider ascent zone tends to increase the PE, and the weaker vertical motion, which leads to less condensation, tends to decrease the PE. The two competing effects result in comparable precipitation to that over the first ridge in the two-ridge run.

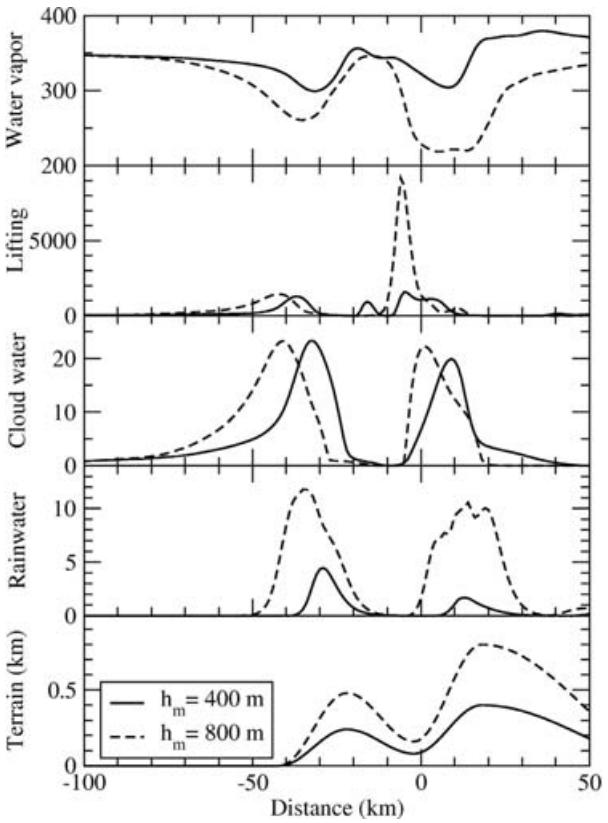


*Fig. 5.* Plots of vertically integrated horizontal water vapour, cloud water, and rainwater fluxes (kg m$^{-1}$ s$^{-1}$), and lifting (defined as $\int_{w>0} \rho w dz$, kg m$^{-1}$ s$^{-1}$) below the freezing level derived from the control simulations with $h_m = 400$ and 800 m, valid at T = 8 h. The vertically integrated horizontal flux is defined as 6 $\rho uqdz$, where q is water vapour, cloud water or rainwater mixing ratio. Terrain is included for reference.

### 4.2. *Evolution of precipitation patterns*

One important question we need to address is whether our simulations can reach steady states, and if the answer is no, how precipitation evolves with time. The time–distance sections of rainwater at the surface, vertical velocity at 2 km ASL, and snow mixing ratio at 4 km (i.e. above the freezing level) derived from three control simulations with $h_m = 200$, 400 and 1200 m, and a reference simulation with $h_m = 400$ m are shown in Fig. 6.

It is evident that for low terrain, the solution reaches a quasi-steady state within 3 hr, after which nearly steady precipitation

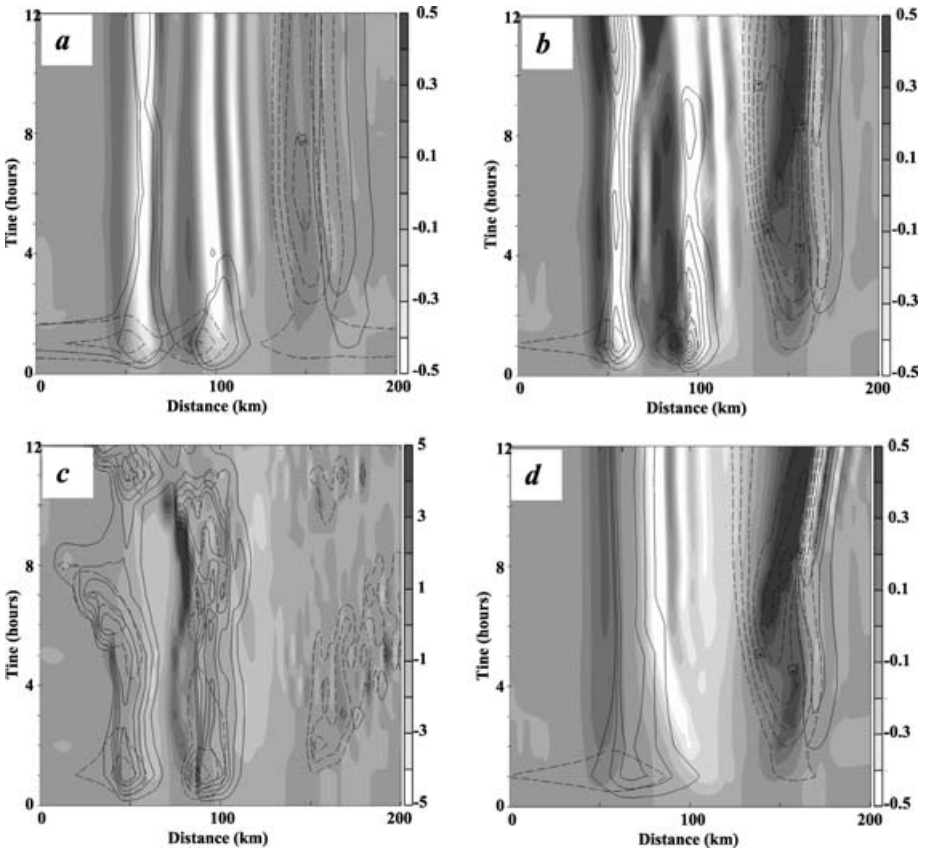


*Fig. 6.* Hovemuller diagram of vertical velocity at 2 km (greyscale), surface rainwater mixing ratio (solid contours), and snow mixing ratio at 4 km (dashed contours) derived from three control simulations corresponding to (a) $h_m = 200$ m with increments of 0.1 m s$^{-1}$ (w), 0.02 g kg$^{-1}$ ($q_r$), and 0.05 g kg$^{1}$ ($q_s$), (b) $h_m = 400$ m with increments of 0.1 m s$^{-1}$, 0.05 g kg$^{-1}$, and 0.1 g kg$^{-1}$, and (c) $h_m = 1200$ m with increments of 1 m s$^{-1}$, 0.05 g kg$^{-1}$, and 0.1 g kg$^{-1}$, respectively. Panel (d) is identical to (b) but derived from the reference ridge simulation with $h_m = 400$ m.

occurs over the upwind slope of the first ridge (Fig. 6a). The vertical motion and lee-wave-related snow mixing ratio reach a quasi-steady state as well. Clearly for higher terrain, no steady state can be reached. For a moderate ridge height, precipitation occurs over the upwind slopes of both the first ridge and the major ridge (Fig. 6b). The updraft at 2 km and rainwater mixing ratio at the surface oscillate in time with a primary period of approximately 5 h, likely due to non-linear wave–wave interaction in the presence of multiple ridges. Additional simulations indicate that the oscillation period is insensitive to the domain size and boundary conditions. In general, a surface rainwater minimum over the major ridge corresponds to a surface rainwater maximum over the narrower ridge and ves versa. It is noteworthy that a few 24 hr simulations have been carried out which show similar oscillations through the integration period. Some aspects of non-linear non-stationary trapped waves induced by a single ridge have been examined by Louisa and Durran (1998). Non-linear wave–wave interactions associated with flow past multiple ridges are currently being investigated (D. Muraki, personal communication, 2006), a thorough study of which is beyond the scope of this research. The strength of the oscillation increases with the ridge height, $h_m$, implying the non-linear nature of the oscillation. The non-linear wave–wave interaction hypothesis is supported by the corresponding reference ridge simulation as well, which shows that the updraft and precipitation reaches a quasi-steady state in approximately 6 h while some non-linear lee waves tend to propagate downstream (Fig. 6d). No quasi-periodic oscillation is observed from single ridge simulations, regardless of the terrain height. For $h_m = 1200$ m, in addition to the oscillation, perturbations over and upstream of the first ridge tend to propagate upstream as shown in both the updraft field and surface rainwater mixing ratio (Fig. 6c). The perturbations weaken while propagating upstream and leave much weaker precipitation over the upwind slope of the first ridge. A few hours later, another precipitation band forms over the windward slope and propagates away. Dynamically, if the vertical extension of perturbations excited by a two-dimensional or quasi-two-dimensional ridge is large enough, the corresponding wave group velocity may exceed the ambient flow speed, and perturbations could propagate upstream away from the terrain (Pierrehumbert and Wyman, 1985). Similar quasi-periodic upstream propagating rain band associated with moist airflow

past concave ridges have been examined by Jiang (2006). It is noteworthy that for $h_m = 1000$ m or higher, the upstream propagation of the precipitation zone occurs in simulations with a single wider reference ridge and still no oscillation is observed.

### 4.3. Precipitation efficiency and non-linearity

To illustrate the variation of precipitation intensity and distribution, the along-stream precipitation rates averaged over 6 h, from T = 6 to 12 h. are shown in Fig. 7 for a range of mountain heights. For low-terrain, precipitation over the first ridge dominates. For $h_m \leq 1000$ m, while precipitation rates over both ridges increase with increasing terrain height, the precipitation increase over the major ridge is faster than over the first ridge (Fig. 7a). The precipitation maxima over the two ridges are comparable around $h_m \sim 700$ m, and for a higher ridge the precipitation rates are larger over the major ridge. When the ridge height is above 1000 m, the precipitation rates over both ridges start decreasing with increasing terrain height. In the mean time, for higher ridges, the precipitation zone over the first ridge tends to extend upstream due to blocking and the upstream propagation of precipitation. Far downstream, the precipitation associated with leeside waves decreases monotonically with increasing mountain height for $h_m \geq 400$ m, likely due to the loss of moisture in the low-level flow over the two-ridge terrain.

Shown in Fig. 7b are the corresponding curves for simulations with the reference ridges. For relatively low terrain, the precipitation rates over the reference ridge are comparable with those over the first ridge of the two-ridge terrain, and are larger for higher terrain. A transition occurs around $h_m = 800$ m, beyond which the precipitation rates start decreasing with increasing terrain height, likely due to blocking. The total precipitation rates integrated over each ridge are shown in Fig. 8a as a function of the mountain height. The corresponding PE over the two ridge wpwind slopes is included in Fig. 8b, which is estimated using $PE_i = \int p\,dx / \int\int \rho w (dq_v/dz)\,dz\,dx$, where $i = 1$ and 2, $PE_1$ and $PE_2$ denote PE over the first and major ridges, respectively, and the nominator and denominator correspond to the total precipitation and condensation rates over the two windward ridge slopes averaged over 6 h (i.e. from T = 6 to T = 12 h). The estimation of the condensation rate is based on Smith (1979) and integrated over areas with updraft only. For $h_m > 1000$, it is difficult to estimate PE due to the upstream propagation of perturbations. A pair of non-linear indices derived from the control simulations are shown in Fig. 9. Based on Figs. 8 and 9, three regimes can be defined, namely, linear, non-linear, and non-linear blocking regimes. For low terrain (approximately $h_m < 300$ m), the wave response is essentially linear (therefore, we refer to this regime as linear regime), as indicated by the linear increase of vertical motion and slow decrease of windward horizontal velocity with

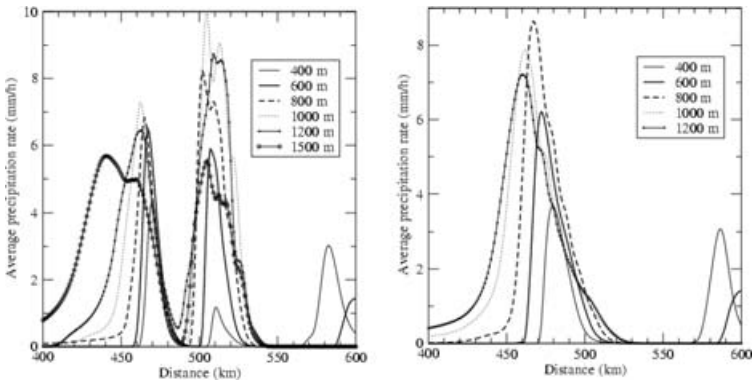


*Fig. 7.* (a) The 6-hr average precipitation rate as a function of along-wind distance, derived from six control simulations with the mountain height $h_m$ varying from 400 to 1500 m. (b) Same as (a) but derived from five reference simulations.

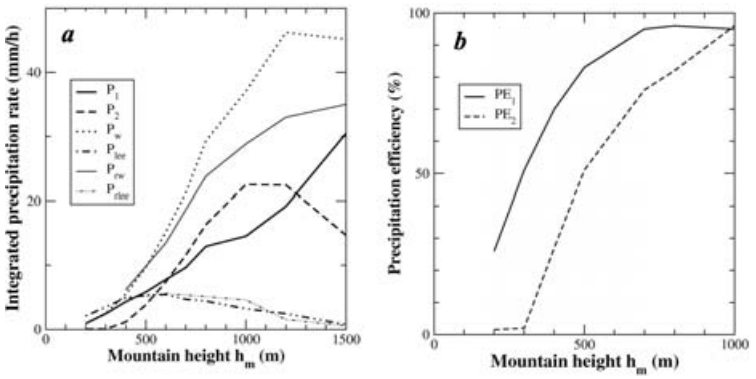


*Fig. 8.* a) The 6 hr average precipitation rates integrated over the windward slopes of the two peaks (denoted as $P_1$ and $P_2$), total precipitation rates integrated over the windward slope and mountain top (i.e. $P_w$), and lee-wave-induced precipitation rates (i.e. $P_{\text{lee}}$) for the control runs and the corresponding reference runs (i.e. $P_{rw}$ and $P_{\text{rlee}}$. (b) Precipitation efficiency over the first and the major ridges estimated from the control runs.

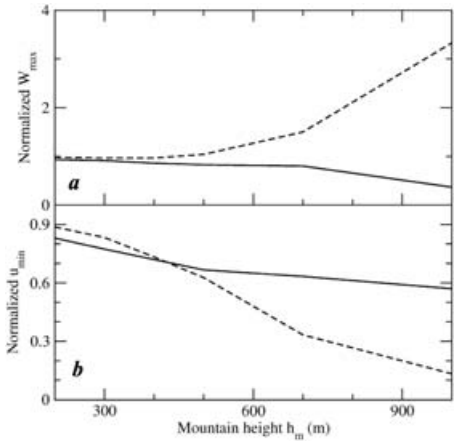


*Fig. 9.* (a) Plot of the maximum updrafts below the freezing level over the windward side of the first ridge (solid) and between the two ridges (dashed) normalized by $U_\circ h_m/a$ versus the ridge height derived from the control runs; (b) plot of horizontal wind minima at the surface normalized by $U_\circ$ over the windward slopes of the first ridge (solid) and the major ridge (dashed) derived from the control set of runs

increasing mountain height (Fig. 9). Most precipitation occurs over the first ridge, and the total precipitation over the two-ridge terrain and the corresponding reference ridge are comparable (Fig. 8a). The PE over the major ridge is virtually zero. For higher terrain, the normalized wave-induced vertical velocity between the two crests become larger than unity, indicating a greater than proportional increase with $h_m$ due to non-linear effect (therefore, referred to as non-linear regime). Accordingly, the total lifting and rainwater over the major ridge increase rapidly with increasing mountain heights (Fig. 5). In fact, a sudden increase of $PE_2$ occurs around $h_m = 300$ m (Fig. 8b), which is qualitatively consistent with Jiang and Smith (2003); according to Jiang and Smith, the upslope precipitation may shut down suddenly as the water content falls below certain threshold, associated with non-linear microphysical processes. The precipitation over the major ridge becomes stronger than over the first ridge for $h_m > 600$ m, largely due to the contribution from the lee-wave-induced updrafts over the major ridge. Consequently, the total precipitation over the two-ridge terrain is larger than over the corresponding reference ridge. For $h_m > 1000$ m, the two-ridge terrain produces approximately 30% more precipitation than the corresponding reference ridge. Through the non-linear regime, the PE over the first ridge is still much larger than that over the major ridge and PE increases significantly with increasing terrain height. The PE over the major ridge increases faster than that over the first ridge and the difference between the two decreases with increasing terrain height accordingly. Again, this is consistent with Jiang and Smith (2003), which argued that the higher condensation rate, the faster the hydrometeor grows. For higher terrain ($h_m > 1000$ m), windward blocking becomes significant (therefore, referred to as non-linear blocking regime) and the total precipitation over the two-ridge terrain starts decreasing due to a sharp decrease of the precipitation over the major ridge. The total precipitation over the first ridge keeps increasing due to the way the total precipitation is computed; the total precipitation over the first ridge is computed by integrating precipitation rates from far upstream to the bottom of the valley between the two ridges.

To understand the relevant dynamics, vertical cross-sections from a pair of control simulations with $h_m = 800$ and 1200 m are shown in Fig. 10. Clearly, for higher terrain, while the upslope ascent increases slowly with the increase of the mountain heights, the amplitude of lee waves increases more dramatically. In the meantime, snow is generated by the lee waves aloft, which becomes rainwater once falling below the freezing level and contributes to precipitation over the upwind slope of the major ridge. Apparently, dominant contribution to the precipitation over the major ridge comes from lee waves excited by the first ridge for relatively high terrain, and hence, the faster increase of precipitation over the major ridge with increasing terrain height is likely due to the non-linear amplification of lee waves in the lee of the first ridge. Note the precipitation rates over the two ridges are comparable for the two examples shown in Fig. 10, but the updraft over the upwind slope of the major ridge is approximately 2.5 times stronger than over the upwind slope of the minor ridge (Fig. 5). Again this is due to the higher PE over the first ridge associated with the longer horizontal dimension of the upstream clouds and the higher water vapour content in the incoming airflow (Fig. 5). For $h_m = 1200$ m, the updraft and precipitation over the upwind slope of the first ridge start to detach from the terrain slope and propagate upstream as illustrated in the previous section.

## 5. Terrain geometry effect

As demonstrated in the previous section, precipitation over multiple ridge terrain is controlled by updrafts and downdrafts induced by each ridge as well as non-linear interaction among gravity waves excited by individual ridges. According to mountain wave theory, the dominant wave characteristics induced by airflow past topography are determined by the atmospheric structure and terrain geometry. In this section, we examine the impact of terrain geometry on the intensity and distribution of precipitation over two-ridge terrain based on simulations with varying ridge height ratio $\alpha$, valley floor height $h_b = \beta h_m$, and inter-ridge distance $d$.

### 5.1. The ridge height ratio $\alpha$

To examine the impact of the ridge height ratio $\alpha$ on precipitation intensity and distribution, simulations have been performed with $\alpha$ varying between 0.1 and 1. We seek answers to the following two questions. First, how sensitive are the precipitation intensity and distribution over two-ridge terrain to the height of the

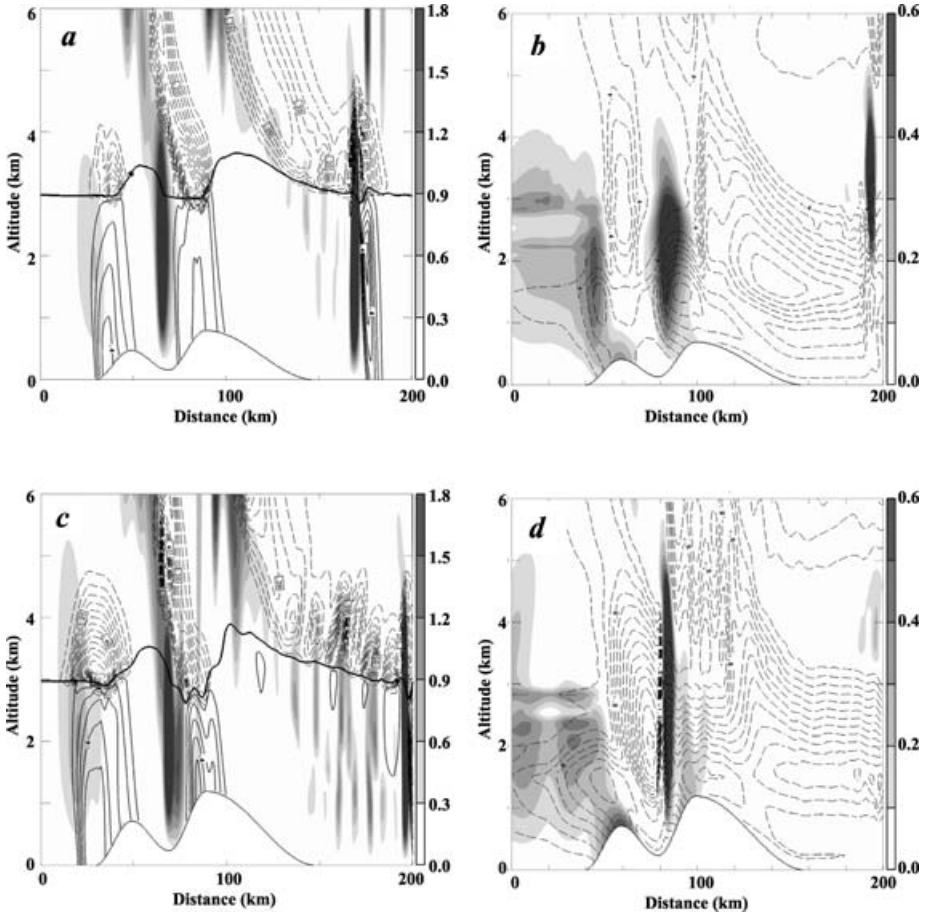


*Fig. 10.* Same as Fig. 4 but for the two control simulations with $h_m = 800$ m (a) and (b) and 1200 m (c) and (d), respectively. In panels (a) and (c), the increments of the updraft, rainwater mixing ratio, and snow mixing ratio are 0.3 m s$^{-1}$, 0.1 g kg$^{-1}$, and 0.05 g kg$^{-1}$

minor ridge? Secondly, if we keep the height of the minor ridge unchanged, how does precipitation vary with increasing height of the major ridge?

Shown in Fig. 11 are precipitation rates averaged over 6 hr from T = 6 to 12 h. as a function of the along-stream distance derived from three simulations with $h_m = 400$ m, $\beta = 0.2$, $d = 2a$, $a = 10$ km, and $\alpha = 0.4$, 0.6, and 0.8, respectively. As expected, precipitation over the first ridge increases with increasing $\alpha$. In the meantime, precipitation over the first ridge tends to shift upstream, likely due to non-linear effect. The averaged precipitation maximum over the major ridge decreases as $\alpha$ increases from 0.4 to 0.6 and increases as $\alpha$ further increases from 0.6 to 0.8. The variation of the precipitation over the major ridge with $\alpha$ is likely due to two competing factors, namely the wave-induced updraft, which increases with increasing $\alpha$ and therefore enhances precipitation, and water vapour loss over the first ridge, which reduces precipitation over the major ridge. Apparently, as $\alpha$ increases from 0.4 to 0.6, the precipitation over the first ridge shows a more than proportional increase, and consequently, the second factor dominates (Fig. 11). As $\alpha$ further increases from 0.6 to 0.8, the increase in precipitation over the first ridge is much

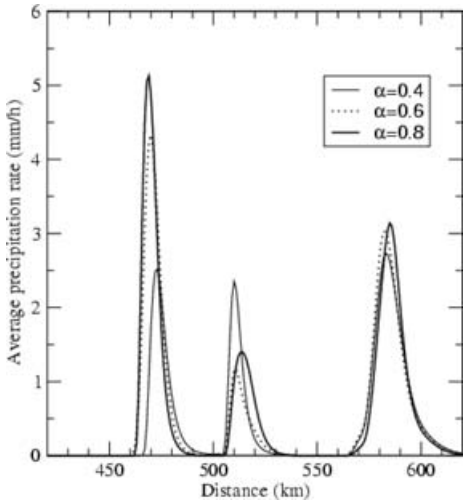


*Fig. 11.* Same as Fig. 7 derived from the control simulation with $h_m = 400$ m and two other simulations with $\alpha = 0.4$ and 0.8, respectively.

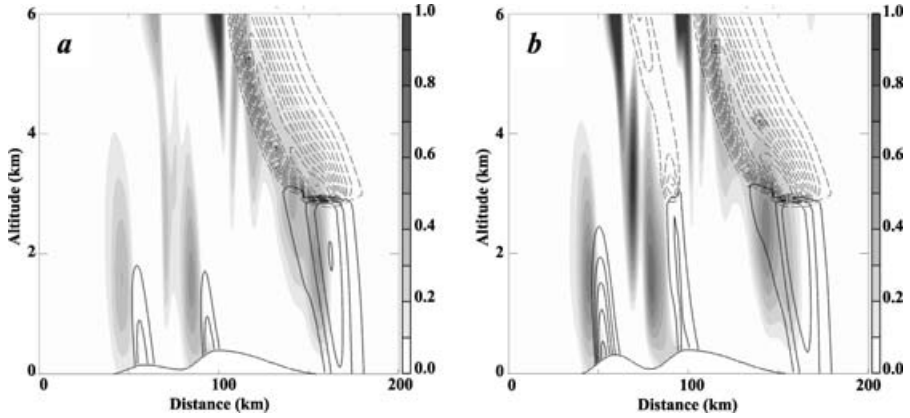


*Fig. 12.* Same as Figs. 4a derived from simulations with $h_m = 400$ m, $\beta = 0.2$, $d = 2a$, and (a) $\alpha = 0.4$ and (b) 0.8, respectively.

less than proportional and the enhancement of precipitation due to the increase of lee waves dominates.

For all three simulations shown in Fig. 11, precipitation over the first ridge is always stronger than over the major ridge, implying higher PE over the first ridge. The difference is smaller for a smaller $\alpha$. In fact, for $\alpha = 0.3$, precipitation over the major ridge becomes slightly larger. In this case, the relative height of the two ridges are 120 and 320 m, respectively. The precipitation over the leeside of the major ridge shows little change as $\alpha$ varies. In another identical set of simulations except for the mountain height $h_m = 800$ m, the increase of the precipitation over the first ridge with $\alpha$ is much smaller than with $h_m = 400$ m and the precipitation over the major ridge increases much more dramatically with increasing $\alpha$, indicating that the contribution from the non-linear lee-wave dominates for higher terrain (Fig. 12).

Shown in Fig. 13 are the averaged precipitation rates derived from three simulations with the first ridge height (i.e. $\alpha h_m$) and the valley floor height (i.e. $h_b = \beta h_m$) fixed as 300 and 200 m, respectively, and the major ridge height ranging from 300 to 1000 m. Correspondingly, $\alpha$ decreases from 1 to 0.3 and $\beta$ decreases from 0.667 to 0.2, respectively. Over the range of parameters examined, stronger precipitation occurs over the first ridge, and precipitation over both ridges tends to increase with increasing $h_m$ (Fig. 13). For $h_m = 300$ and 500 m, there is little precipitation over the major ridge, and for $h_m = 1000$ m, the precipitation over the two ridges becomes comparable implying a possible bifurcation behavior as illustrated by Jiang and Smith (2003). Further downstream, wave-induced precipitation decreases with increasing $h_m$. The related dynamics can be interpreted using Fig. 14. The updraft is extremely weak over the major ridge for $h_m = 300$ m, and so are lee-wave-induced updrafts between the two ridges. It is interesting that the updraft over the upwind slope of the first ridge and the lee-wave-induced updrafts in the lower troposphere increase with increasing $h_m$ even though the height of the first ridge is unchanged, indicating that for two-ridge terrain, updrafts are not only determined locally by the terrain underneath and upstream, but also influenced by terrain downstream, likely through wave–wave interactions.

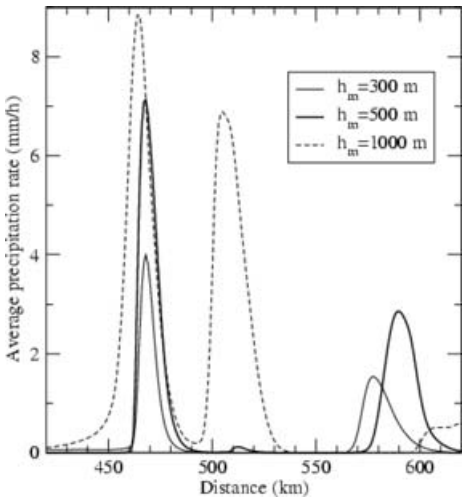


*Fig. 13.* Same as Figs. 7 and 11 but derived from three simulations corresponding to $\alpha h_m = 300$ m, $h_b = 200$ m, $h_m = 300$, 500 and 1000 m.

It is evident that with a higher major ridge, the updraft over the upwind slope of the first ridge is stronger, wider, and the vertical extension is larger. Consequently, snow forms above the freezing level and contributes to precipitation over both ridges.

### 5.2. *Valley floor depth*

According to linear theory, a deeper valley increases the relative height of the major ridge and therefore increases the total upslope ascent. In addition, previous studies also suggested that wave response could be stronger over a steeper slope (Miller & Durran, 1991). To examine the impact of the valley depth on precipitation, a set of simulations have been carried out with $h_m = 400$ m, $\alpha = 0.6$, $d = 2a$, and the valley factor $\beta = 0$, 0.4, and 0.6, respectively. Compared with the control simulation, the deeper valley simulation (i.e. $\beta = 0$) produces much stronger precipitation over the major ridge and much weaker precipitation over the first ridge (Fig. 15). For a shallower valley (i.e. $\beta > 0.2$),

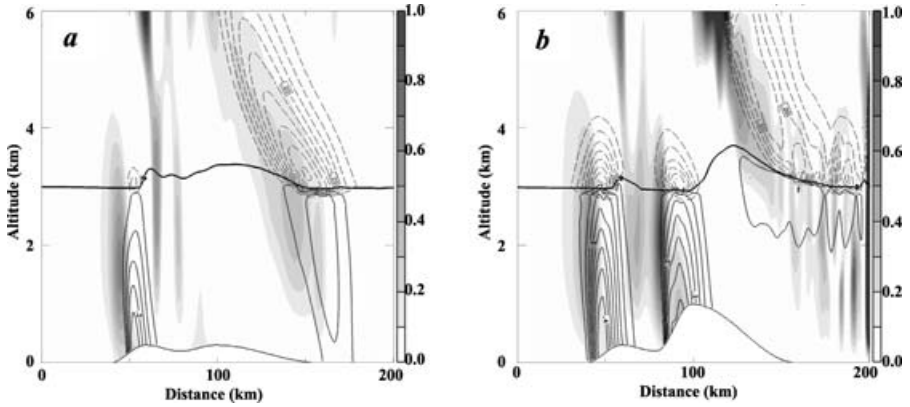


*Fig. 14.* Same as Fig. 12 but derived from two simulations corresponding to $\alpha h_m = 300$ m, $h_b = 200$ m, and $h_m = 300$ and 1000 m.

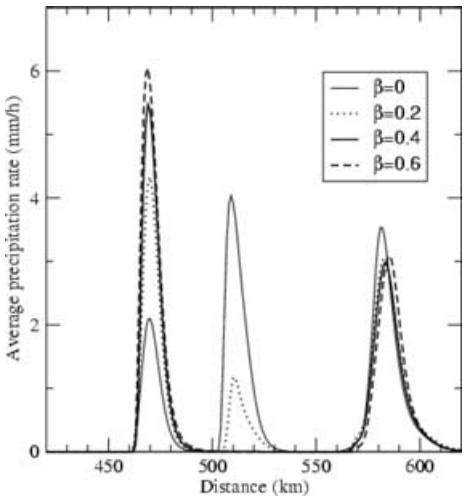


*Fig. 15.* Same as Figs. 7 and 11 but derived from the control simulations with $h_m = 400$ m and other three simulations sensitivity test runs with $\beta = 0$, 0.4 and 0.6.

precipitation over the major ridge becomes practically zero, and stronger precipitation occurs over the first ridge.

Vertical sections corresponding to $\beta = 0$ and $\beta = 0.6$ (i.e. $\alpha - \beta = 0$) are shown in Fig. 16. For $\beta = 0$, the updraft over the major ridge is considerably stronger than over the first ridge, and the precipitation is more intense accordingly (Fig. 16). For $\beta = 0.6$, the valley between the two ridges vanishes and the updraft over the major ridge is much weaker than with $\beta = 0$. Over the first ridge where strong precipitation occurs, the updraft is much stronger and the updraft zone is wider than with $\beta = 0$.

In general, the total precipitation over the two-ridge terrain is larger for a deeper valley (i.e. a smaller $\beta$). The increase in total precipitation due to the decrease of $\beta$ is proportionally larger for higher terrain due to non-linear wave amplification.

### *5.3. Inter-ridge distance*

According to (1), for a larger inter-ridge distance, the horizontal dimensions of the lee slope of the first ridge and the upwind slope of the major ridge are larger, which may weaken low-level vertical motion, as w near the surface is proportional to the terrain slope. On the other hand, the increase of the upwind slope length of the major ridge may increase PE through increasing the advection time. As an example, results from two simulations corresponding to $d = a$ and $d = 3a$ are shown in Figs. 17 and 18. Compared to the corresponding control simulation (i.e. $d = 2a$, included in Figs. 18 and vertical section shown in Fig. 4a), the simulation with $d = a$ produces less precipitation over the major ridge, although the updraft over the major ridge is much stronger, likely due to the relatively small horizontal dimension of the updraft. Consequently, the advection time is too short for hydrometeors to grow into precipitable sizes. For the simulation with $d = 3a$, the horizontal dimension of the updraft is about twice as large as with $d = a$, and more precipitation occurs over the major ridge accordingly. For an identical set of simulations except for $h_m = 800$ m, the averaged precipitation over the major ridge is much less sensitive to the variation of $d$ as the non-linear wave amplification becomes important and the increase of updraft due to the decrease of $d$ cancels out the effect of the advection time decrease.

It is noteworthy that for relatively high terrain, the period of precipitation oscillation illustrated in the previous section varies with $d$; specifically, the larger the distance, the longer the oscillation period. Therefore, even though the precipitation over the first ridge derived from the simulation with $d = 3a$ is twice as much as wth $d = a$ at T = 8 h. (Fig. 18), the averaged precipitation rates from the two simulations over the first ridge are comparable (Fig. 17).

## 6. Summary

In this model-based study, two-dimensional simulations have been carried out with a narrower ridge superposed on the upwind slope of a wider ridge to deepen our understanding of orographic precipitation over complex terrain with multiple ridges and multiple horizontal scales. A variety of interactions between perturbations launched from the two ridges have been

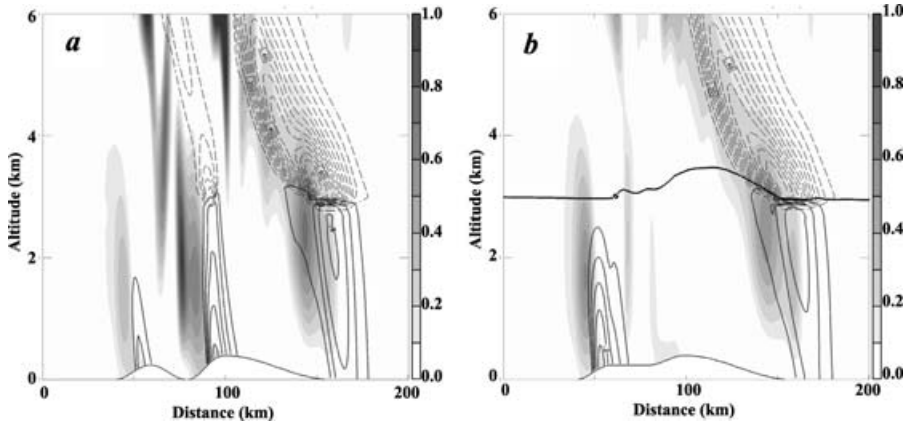


*Fig. 16.* Same as Figs. 12 and 14 but derived from two simulations corresponding to $h_m = 400$ m and $\beta = 0$ and 0.6, respectively. Other terrain parameters are identical to the control set of simulations.

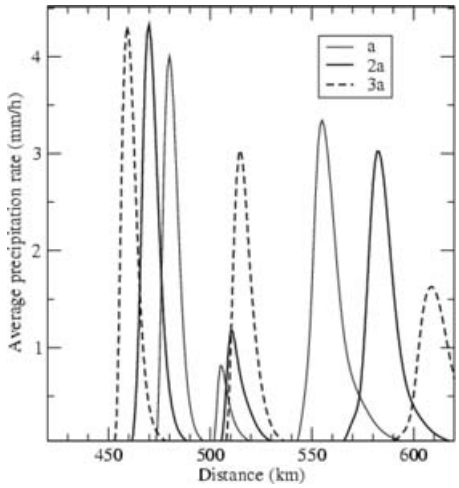


*Fig. 17.* Same as Figs. 7, 11 and 15, but derived from the control simulation with $h_m = 400$ m and two simulations with $d = a$ and $3a$, respectively.

identified. The minor ridge is found to have significant impact on precipitation over the major ridge mainly through two pairs of competing processes, namely the dynamical and microphysical pairs. The dynamical pair includes decent over the lee slope of the first ridge, which tends to reduce PE by deceasing the horizontal dimension of the updraft zone over the upwind slope of the major ridge, and lee waves excited by the first ridge, which may enhance the updraft over the major ridge and contribute to precipitation. The microphysical pair includes the reduction of water vapour content in the airflow that reaches the major ridge due to precipitation over the first ridge, which tends to reduce precipitation, and cold cloud formation above the upwind slope of the major ridge, associated with lee waves excited largely by the first ridge, which tend to enhance precipitation underneath.

The relative importance of these processes strongly depends on the terrain geometry, especially the ridge heights. Based on the control set of simulations, three dynamical regimes have been identified, namely linear, non-linear, and blocking regimes. If the terrain is low, the wave response is essentially linear, and more precipitation falls over the upwind slope of the first ridge even if the first ridge is significantly lower than the major ridge. In this regime, lee waves are too weak to generate precipitable cold clouds and their contribution to precipitation is relatively insignificant. On the other hand, due to the descent over the first ridge, the horizontal dimension of the updraft zone over the major ridge is relatively small. Consequently, the advection time, the time for hydrometeors to grow, is relatively short, and accordingly the PE is smaller. The precipitation over the major ridge is further reduced by the reduction of water vapour in the low level air flow due to the precipitation over the first ridge. As a result, the total precipitation over the two-ridge terrain is about the same or smaller than over the wider smooth reference ridge. For higher ridge, lee waves between the two ridges can be significantly stronger due to non-linear wave amplification. The updrafts associated with the lee waves excited by the first ridge have significant contribution through either directly producing condensation below the freezing level or generating cold clouds above the freezing level. As a result, precipitation over the two ridges are comparable and the total precipitation can be significantly larger than over the corresponding reference ridge. In this regime, non-linear wave–wave interaction also causes quasi-periodic oscillation of precipitation over the two ridges with precipitation maxima alternating between the two ridges. In the blocking regime ($M > 1$), windward blocking becomes significant and precipitation over the upwind slope of the first ridge tends to propagate upstream.

Additional simulations indicate that the intensity and distribution of precipitation over the two-ridge terrain are sensitive to the ridge height ratio, $\alpha$, valley parameter $\beta$, and inter-ridge distance $d$ as well. For relatively low terrain with a fixed major ridge height, the increase of the first ridge height tends to increase precipitation over the first ridge and the precipitation over the major ridge may increase or decrease, depending on which of the two competing factors dominates, the increase of

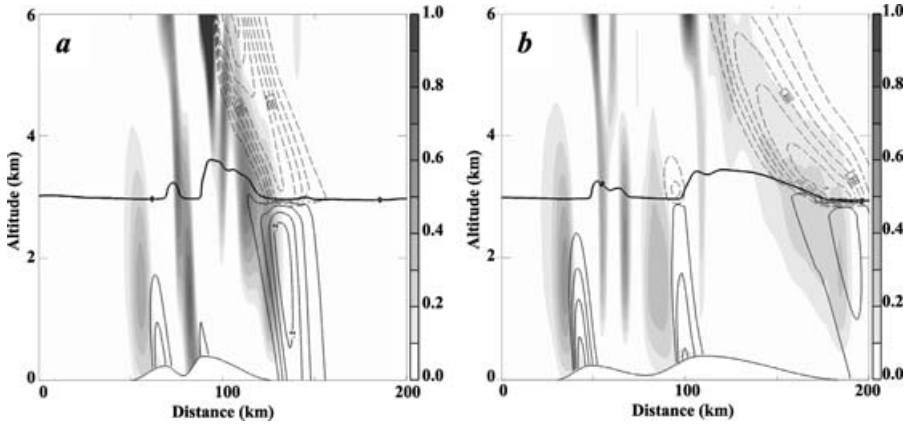


*Fig. 18.* Same as Figs. 12, 14 and 15 but derived from two simulations corresponding to $h_m = 400$ m, and $d = a$ and $3a$, respectively. Other terrain parameters are identical to the control set of simulations.

lee-wave-induced updraft over the major ridge and the reduction of water vapour in the low-level airflow due to precipitation over the minor ridge. For high terrain (∼800 m or higher), non-linear wave amplification dominates and a higher minor ridge produces more precipitation over the major ridge. In general, with a higher minor ridge, the two-ridge terrain tend to drain more water vapour out of the low-level airflow. If we keep the first ridge height unchanged, the increase of the major ridge height is found to enhance precipitation over both ridges, implying that the low-level updrafts are not only controlled locally by the terrain underneath and upstream, but also influenced by the terrain shape downstream.

A deeper valley between the two ridges tends to increase precipitation over the major ridge due to the increase of the relative height of the major ridge, and decrease precipitation over the first ridge as the updraft over the first ridge is stronger with a larger $\beta$. Overall, a deeper valley tends to increase the total precipitation over the two-ridge terrain, especially for high terrain. We also find that the period of oscillation increases with increasing inter-ridge distance. Over the range of parameters examined, terrain with a larger inter-ridge distance tends to produce more precipitation over the major ridge.

At last, although a variety of interactions between perturbations excited by the two ridges have been identified in this study, apparently we could not provide complete answers to the questions we raised in the introduction. Our simulations only cover a relatively small parameter space in terms of both terrain geometry and the atmosphere. In addition, boundary layer effect is not included in this study. Clearly, further studies are needed to test these conclusions over a broader range of atmosphere and terrain parameter spaces.

## 7. Acknowledgments

The author thanks Drs. Ron Smith and James Doyle for their constructive comments and suggestions. This research was supported by the Office of Naval Research (ONR) program element 0601153N. The simulations were made using the Coupled Ocean/Atmospheric Mesoscale Prediction System (COAMPS) developed by US Naval Research laboratory.

## References

Bergeron, T. 1949. The problem of artificial control of rainfall on the globe. Part II: The coastal orographic maxima of precipitation in autumn and winter. *Tellus* **1**, 15–32.

Bougeault, P., Binder, P., Buzzi, A., Dirks, R., Houze, R., and Coauthors, 2001. The MAP special observing period. *Bull. Amer. Meteor. Soc.* **82**, 433–462.

Bruitjes, R. T., and Hall, W. 1994. Interactions between topographic airflow and cloud and precipitation development during the Passage of a Winter Storm in Arizona. *J. Atmos. Sci.* **51**, 48–67.

Chen, S.-H. and Lin, Y.-L. 2005. Effects o moist Froude number and CAPE on a conditionally unstable flow over a mesoscale mountain ridge. *J. Atmos. Sci.* **62**, 331–350.

Chiao, S., Lin, Y.-L. and Kaplan, M. L. 2004. Numerical study of orographic forcing of heavy orographic precipitation during MAP-IOP-2B. *Mon. Wea. Rev.* **232**, 2184–2203.

Colle, B. A. 2004. Sensitivity of orographic precipitation to changing ambient conditions and terrain geometries: an idealized modeling perspective. *J. Atmos. Sci.* **61**, 588–606.

Colle, B. A. and Zeng, Y. 2004. Bulk microphysical sensitivities within the MM5 for orographic precipitation. Part II: impact of barrier width and freezing level. *Mon. Wea. Rev.* **132**, 2802–2815.

Emanuel, K. A. 1994. *Atmospheric Convection*. Oxford University Press, New York, 580 pp.

Fuhrer, O. and Schär, C. 2005. Embedded cellular convection in moist flow past topography. *J. Atmos. Sci.* **62**, 2810–2828.

Hodur, R. M. 1997. The Naval Research Laboratory's Coupled Ocean/Atmosphere Mesoscale Prediction System (COAMPS). *Mon. Wea. Rev.* **125**, 1414–1430.

Jiang, Q. 2003. Moist dynamics and orographic precipitation. *Tellus* **55A**, 301–316.

Jiang, Q. 2006. Precipitation over concave terrain. *J. Atmos. Sci.* **63**, 2269–2288.

Jiang, Q. and Smith, R. B. 2003. Cloud timescale and orographic precipitation. *J. Atmos. Sci.* **60**, 1534–1559.

Kessler, E. 1969. On the distribution and continuity of water substance in atmospheric circulations. *Meteor. Monogr.* **32**, Amer. Meteor. Sco., 84pp.

Kirshbaum, D. J. and Durran, D. R. 2004. Factors governing cellular convection in orographic precipitation. *J. Atmos. Sci.* **61**, 682–698.

Lalas, D. P. and Einaudi, F. 1974. On the correct use of the wet adiabatic lapse rate in the stability criteria of a saturated atmosphere. *J. Appl. Meteor.* **13**, 318–324.

Louisa, B. N. and Durran, D. R. 1998. A modeling study of nonstationary trapped mountain lee waves. Part II: Nonlinearity. *J. Atmos. Sci.* **49**, 1427–1442.

Medina, S. and Houze R. A. Jr. 2003. Air motions and precipitation growth in Alpine storms. *Quart. J. R. Meteor. Soc.* **129**, 345–372.

Miglietta, M. M. and Buzzi, A. 2004. A numerical study of moist stratified flow regimes over isolated topography. *Quart. J. R. Meteor. Soc.* **130**, 1749–1779.

Miller, P. P. and Durran, D. R. 1991. On the sensitivity of downslope windstorms to the asymmetry of the mountain profiles. *J. Atmos. Sci.* **48**, 1457–1473.

Pierrehumbert, R. T. and Wyman, B. 1985. Upstream effects of mesoscale mountains. *J. Atmos. Sci.* **42**, 977–1003.

Rotunno, R. and Ferretti, R. 2001. Mechanisms of intense Alpine rainfall. *J. Atmos. Sci.* **58**, 1732–1749.

Rotunno, R. and Ferretti, R. 2003. Orographic effects on rainfall in MAP cases IOP 2b and IOP 8. *Quart. J. R. Meteor. Soc.* **129**, 373–390.

Rutledge, S. A. and Hobbs, P. V. 1983. The mesoscale and microscale structure and organization of clouds and precipitation in midlatitude cyclones. VIII: A model for the "seeder-feeder" process in warm-frontal rainbands. *J. Atmos. Sci.* **40**, 1185–1206.

Rutledge, S. A. and Hobbs, P. V. 1984. The mesoscale and microscale structure and organization of clouds and precipitation in midlatitude cyclones. XII: a diagnostic modeling study of precipitation development in narrow cold-frontal rainbands. *J. Atmos. Sci.* **41**, 2949–2972.

Schneidereit, M. and Schär, C. 2000. Idealised Numerical Experiments of Alpine Flow Regimes and Southside Precipitation Events. *Meteorol. Atmos. Phys.*, **72**, 233–250.

Schultz, P. 1995. An explicit cloud physics parameterization for operational numerical weather prediction. *Mon. Wea. Rev.* **123**, 3331–3343.

Scorer, R. S. 1949. Theory of lee waves of mountains. Quart. *J. Roy. Meteor. Soc.* **75**, 41–56.

Smith, R. B. 1979. The influence of mountains on the atmosphere. *Adv. Geophys.* **21**, 87–230.

Smith, R. B. 1980. Linear theory of stratified hydrostatic flow past an isolated mountain. *Tellus* **32**, 348–364.

Smith, R. B. and Barstad, I. 2004. A linear theory of orographic precipitation. *J. Atmos. Sci.* **61**, 1377–1391.

Smith, R. B. and Lin, Y.-L. 1982. The addition of heat to a stratified airstream with application to the dynamics of orographic rain. *Quart. J. R. Met. Soc.* **108**, 353–378.

Smith, R. B., Jiang, Q., Fearon, M. G., Tabary, P., Dorninger, M., Doyle, J. D. and Benoit, R. 2003. Orographic precipitation and airmass transformation: An Alpine example. *Quart. J. R. Meteor. Soc.* **129**, 433–454.

Smith, R. B., Barstad, I. and Bonneau, L. 2005. Orographic precipitation and Oregon's climate transition. *J. Atmos. Sci.* **62**, 177–191.

Stoelinga, M. T., Hobbs, P. V., Mass, C. F., Locatelli, H. D., Colle, B. A. and coauthors, 2003. Improvement of microphysical parameterization through observational verification experiment. *Bull. Amer. Met. Soc.* **84**, 1807–1826.